X-RAY MICROSCOPY

X-ray microscopy is not a new field, with the first work dating back to the beginning of the twentieth century. The first instruments were simple indirect transmission microscopes. A common technique was contact microradiography and involved placing a photographic film in contact with a sample and then illuminating the sample with X rays to produce a shadowgraph. The image was then magnified using an optical microscope. This technique, when modified to allow projection of the object onto the film instead of having the film in contact with the sample, produced a 0.1 μm resolution by the 1950s. Contact microscopy, in which the film is replaced by a photosensitive material, was the next natural development. Both classical X-ray microscopy techniques continue to be used in medical and biological research and have produced some spectacular images of samples ranging from chromosomes to brain tissue (1,60,61).

The question may arise then why a 0.1 μm resolution for modern day X-ray microscopes (XRMs) should be counted as an important achievement. The reason is that today's XRMs are capable of doing many more types of experiments than the previous generation microscopes could. Although they lost ground to the high resolution scanning electron microscope (SEM) in the 1960s and later to the atomic resolution scanning tunneling microscope (STM) in the 1980s, XRMs have recaptured the interest of the scientific community because they are capable of unique experiments not possible with other microscopes. High intensity broad-band X rays generated as synchrotron radiation (62,63), improved optics and instrumentation, the ability to study radiation-sensitive and wet samples with soft X rays, and the ability to do spectroscopic imaging make today's X-ray microscopes extremely versatile (64–67). The 0.1 μm resolution record has also been broken by several X-ray microscopes.

Many interesting effects—both basic and technological—are observed in the dimensional range of approximately 50 nm to 5 μm. This region bridges the nanostructure domain with the macroscopic world and contains aspects of both. A typical case is that of integrated circuit (IC) development, where today the critical dimension (CD) is approaching 0.1 μm. X-ray microscopes are ideally suited to the study of systems in that size range, from untreated biological samples to semiconductor heterostructures. They can yield information about local variations in chemical composition and electronic structure through spatially resolved absorption, fluorescence, and photoelectron spectra. One speaks often of *spectromicroscopes,* not just microscopes. The word *spectromicroscopy* combines aspects of spectroscopy and microscopy as does the word *microspectroscopy*. However, it is the last four syllables of either expression that describe the thrust of either technique. Thus, spectromicroscopic measurements entail taking images containing partial spectral information of small areas. Typically a larger energy band pass is selected to allow for a sufficiently high count rate to allow image acquisition in reasonable time. Microspectroscopic measurements involve acquiring spectroscopic data with partial spatial information. In this incarnation it is common to collect a high resolution spectrum from an area of the image by either counting for a longer time or using a larger area. The two techniques are frequently used in unison. Given a high X ray flux, it is even possible to use both techniques simultaneously, collecting an energy spectrum for each pixel of the image.

In 1994, Moewes catalogued the world's VUV and X-ray microscopes, listing 42 such instruments, 25 of which use synchrotron radiation (2). The extreme vacuum ultraviolet (VUV) region extends from 2 Å to 1000 Å (12 eV to 6200 eV). Of this, the range from 20 Å to 500 Å (25 eV to 620 eV) is often called the soft X-ray region. In the hard X-ray region, the wavelength ranges from 0.5 Å to 2 Å (the energy from 6.2 keV to 25 keV) (3). Since then, however, more X-ray microscopes have come into existence, in particular at new third-generation synchrotrons such as the Advanced Light Source of the Lawrence Berkeley National Laboratory and the Sincrotrone Trieste in Trieste, Italy. Spectromicroscopy programs are in the genesis stage at budding synchrotrons such as the Advanced Photon Source in Illinois and the Synchrotron Radiation Research Center in Hsinchu, Taiwan. Any of these light sources is a site of choice for building a X-ray spectromicroscope because of the high brightness available. There are also efforts to use plasma X-ray sources for microscopy (4). These sources are inherently limited in light output, but they do allow experiments to be done away from synchrotrons.

Most modern X-ray microscopes, though varying widely in their optics and signal collected, can be divided into two broad categories: *imaging* and *scanning.* Both types, in their transmission and emission incarnations, will be described in this article. Indirect techniques such as Fourier-transform X-ray holography will not be discussed.

INTERACTION OF X RAYS WITH MATTER

It would not be appropriate to treat in depth here a topic on which books have been written. We will confine our discussion of the interaction of X rays with matter to the cases that directly concern the operation of X-ray spectromicroscopes, with an emphasis on photoemission in solids.

Surface Sensitivity

Nondiffractive optics for X rays only work at glancing angles. This fact follows from the calculation of the reflectivity of light at an interface using the Fresnel equations. Only a glancing angle produces a significant reflectivity for X-ray wavelengths. X rays are not simply reflected off the top surface of the material under study. In fact, it is important to know how far the X rays penetrate into the sample in order to understand what fraction of the sample contributes to the signal collected, and thus, what part of the sample we are really studying. This can be arrived at through consideration of the absorption coefficients of the materials composing the sample. The absorption coefficient α is a function of the photon energy $\hbar\omega$, and the intensity at a distance z inside the material can be written as

$$I = I_0 e^{-\alpha z} \tag{1}$$

where I_0 is the intensity incident on the surface. The photon attenuation length λ_{ph} (also called the photon mean free path) is $1/\alpha$ and is commonly used as a measure of how far the photons penetrate into the sample (although the intensity at that distance is about 37% of the incident intensity). λ_{ph} is a function of photon energy and varies for different substances

J. Webster (ed.), *Wiley Encyclopedia of Electrical and Electronics Engineering.* Copyright © 1999 John Wiley & Sons, Inc.

because of differences in material characteristics. For instance, at a photon energy of 100 eV, λ_{ph} is 0.18 μm for carbon and 0.11 μm for molybdenum, yet at 1000 eV it is 1.9 μm for carbon and 0.19 μm for molybdenum, and at 5000 eV it is 234.1 μm for carbon and 1.8 μm for molybdenum. Clearly, for transmission X-ray microscopes rather thick samples may be used, with local differences in the absorption coefficient of the sample providing a contrast mechanism. Photoemission microscopes rely on the photoelectrons ejected from the sample for their signal. As illustrated in Fig. 1, photoelectrons (and Auger electrons) are excited everywhere the X rays can reach in the sample, but because of electron scattering, only those electrons excited within the (isotropic) electron mean free path λ_e of the sample surface can escape from the sample. This is why photoemission spectroscopy (PES) is a *surface-sensitive* technique. λ_e, a function of the electron kinetic energy (approximately proportional to the square root of the kinetic energy) that also varies for different materials, varies from about 5 Å to 100 Å for kinetic energies from 2 eV to 130 eV, (5), a range of interest for the University of Wisconsin spectromicroscope MAXIMUM. Because of this ability to sample only the top layers of a material, PES is an ideal technique for the study of surfaces and interfaces. It is also possible to design a microscope that collects the photoelectrons emitted from the opposite side of a thin sample that is illuminated with X rays, thus combining transmission and emission X-ray microscopy (6).

Photoemission

To explain the photoemission process, it is useful to examine the band structure of a solid. A photon of energy $\hbar\omega$ excites an electron in a valence band state of energy E_i into an unoccupied state of energy E_f in the conduction band and leaves behind a hole. We have

$$E_f = E_i + \hbar\omega \tag{2}$$

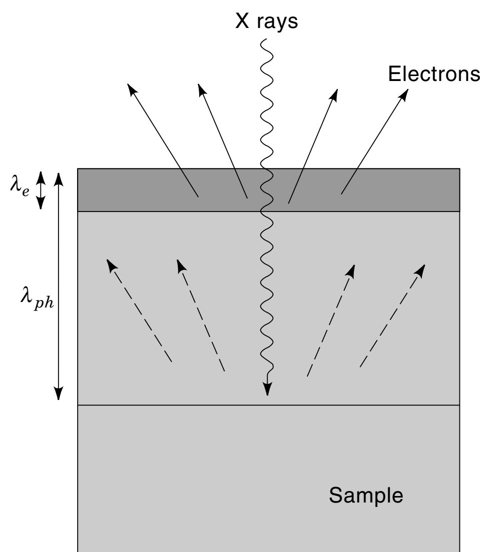

Figure 1. Schematic showing the surface sensitivity of photoemission. Although X rays penetrate to a depth of λ_{ph} in the sample, only those photoelectrons excited within the electron escape depth λ_e are emitted from the sample.

If E_f is sufficient to overcome the material's photoionization potential or work function ϕ, the electron energy is above the vacuum level E_{vac} given by $E_v + \phi$, where E_v is the energy of the top of the valence band (and is identical to the Fermi energy $\mathscr{E}_F$ in a metal), the photoelectron can escape into vacuum. This electron is said to have been *photoemitted.* Subtracting E_{vac} from Eq. (2), we obtain

$$E_f - E_{vac} = E_i + \hbar\omega - (E_v + \phi) \tag{3}$$

$$= \hbar\omega - (E_v - E_i) - \phi \tag{4}$$

Because $E_f - E_{vac}$ is the photoelectron kinetic energy E_{kin} and $E_v - E_i$ is the binding energy E_b of the electron in the solid, we may rewrite Eq. (4) as

$$E_{kin} = \hbar\omega - E_b - \phi \tag{5}$$

E_{kin} is the value measured in a photoemission experiment. In an experimental system, assuming that the electron energy analyzer and the sample are in equilibrium, ϕ in Eq. (5) will be the work function of the analyzer, which is typically higher than the sample work function. (Because the analyzer's vacuum level is not the same as the sample's (although the Fermi level is), it can only detect electrons with a kinetic energy above its own threshold). This difference also leads to the secondary electron peak being cut off at its lower energy end.

Not all transitions from E_i to E_f are allowed. In the absence of spin-orbit interaction, only those transitions that obey the dipole selection rules

$$\Delta l = \pm 1 \tag{6}$$

$$\Delta m = 0 \pm 1 \tag{7}$$

are permitted, where l is the azimuthal or orbital angular momentum quantum number and can take on the values 0, 1, 2, . . ., $n - 1$ (where n is the principal quantum number), and m is the magnetic quantum number and ranges from $-l$ to l. If a spin-orbit intersection exists, as it does for metals, the total angular momentum quantum number $j = l \pm \frac{1}{2}$ gives rise to a splitting in the binding energy. Such a split for the Al 2p core level can be seen in the electron energy distribution curve (EDC) in Fig. 2. In EDCs there is also a large diffuse peak near 0 eV kinetic energy, which is the secondary electron background and results from electrons that have lost energy through inelastic scattering from other electrons. Core levels of low kinetic energy will be seen riding on top of this background.

See also the article PHOTOEMISSION in this Encylopedia.

Photoemission: Applications. There are various experimental techniques that use photoemission. Examples include angle-resolved photoemission spectroscopy (ARPES), extended X-ray absorption fine structure (EXAFS) and its cousins SEXAFS (S for surface) and NEXAFS (N for near edge), and, of course, electron spectroscopy for chemical analysis (ESCA) and X-ray photoelectron spectroscopy (XPS). ESCA and XPS are essentially the same physical technique, as are EXAFS and NEXAFS, with the difference in nomenclature arising from the application. We shall refer to them as *X-ray photoemission* and *X-ray absorption,* respectively. In the former, the occupied valence band and deeper states are probed by using a fixed photon energy and examining the distribu-

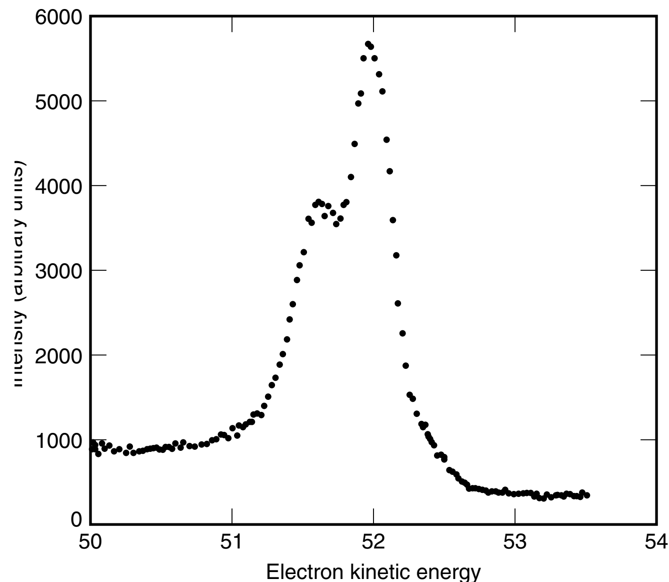

Figure 2. EDC from MAXIMUM showing spin–orbit splitting of the Al $2p$ core level.

tion of photoelectron kinetic energies (the EDC). In the latter, unoccupied conduction band states are explored by scanning the photon energy and collecting the photoelectrons in total yield mode as a function of photon energy. In both photoemission and photoabsorption modes the aim of spectromicroscopy is to distinguish between chemical states on a microscopic scale. This can be done by studying chemical shifts of electronic levels corresponding to specific materials comprising the sample.

Chemical Shifts. Core level electrons are tightly bound to their atoms and thus serve well as a means of elemental identification. Variations in local chemistry induce local charging and hence *shifts* in the core level binding energies, which are reflected in the photoelectron spectra.This happens because of changes in the screening of the nucleus by the valence electrons. For example, if the atom of interest is in a chemical environment that results in additional valence electrons being drawn to the atom, Coulomb screening will increase and the binding energy of the core level will be decreased. If, however, the atom is bonded to a highly electronegative material, its oxidation state will change and the number of valence electrons screening the core will be decreased, resulting in a corresponding increase in the core level binding energy. The effects on binding energy are more complicated in the case of nonionic bonding. Shifts from pure elemental values have been observed for several compound materials. The amount and sign of the shift can be quantified in a straightforward way for the chemical shift $\Delta E_n(A, B)$ for atom n in two different chemical environments A and B by the following equation (7):

$$\Delta E_n(A,B) = \left(\frac{q_n^A}{\bar{r}_{\mathrm{v},n}^A} - \frac{q_n^B}{\bar{r}_{\mathrm{v},n}^B}\right) + (V_n^A - V_n^B) \quad (8)$$

$\bar{r}_{\mathrm{v},n}$ is the average radius of the valence shell of the nth atom, and the q_n are screening charges. Thus the first term is the difference in screening potential between environments A and B. The second term is the difference in the Madelung potentials of A and B, where for V_n we may write

$$V_n = \sum_{n \neq n'} \frac{q_n}{R_{nn'}} \quad (9)$$

Here we sum over all surrounding ionic charges q_n centered at positions $R_{nn'}$ measured with respect to the atom n. Equation (8) has been shown to be a simple but good predictor of chemical shifts in solids.

Other Spectral Features. Photoelectron spectra exhibit features not solely ascribable to primary and secondary electrons. The lineshape, for example, is not a delta function, but is broadened. Taking into account the finite lifetime of the hole created by photoexcitation of a core level electron, the theoretical lineshape should be a Lorentzian with width inversely proportional to the core lifetime. There is also a further broadening caused by electron–phonon scattering. In real life, the shape is not a Lorentzian, but is convoluted with a Gaussian arising from instrumental limits such as detector energy resolution, monochromator resolution, the Doppler effect, and thermal broadening. The resulting lineshape is called a Voigt function and is extensively used in spectroscopy.

The hole can decay via radiative or Auger recombination. In the former case, an electron from a higher energy level drops down into the vacancy, and radiation with an energy corresponding to the difference between the levels is emitted and is called fluorescence. Luminescence refers to visible or UV light emitted from valence transitions. Both kinds of light can be used as chemical signatures for spectromicroscopy, as they are for two of the X-ray microscopes discussed in this article. This photon emission that accompanies photoemission, though it is not as surface-sensitive, can be exploited in a manner analogous to energy dispersive analysis of X rays (EDAX) in a scanning electron microscope (SEM) to acquire images mapping elements on the sample.

In the Auger process, the energy difference is used to ionize a higher-level electron. This Auger electron is ejected with a kinetic energy characteristic of the material in question. There is a finite set of permitted Auger transitions for a given element, and Auger peaks are independent of photon energy under nonresonance conditions.

Plasmons occur in metals in a series, with the plasmon peaks shifted from the core peak to lower kinetic (higher binding) energies by multiples of $\hbar\omega_{\mathrm{p}}$, the plasma frequency, if $\omega > \omega_{\mathrm{p}}$. Thus plasmons are a form of energy loss for primary electrons. The conduction band electrons in a metal form an electron gas that can be set into collective oscillation by an excited photoelectron. A plasmon represents one quantum of this oscillation.

Excitons can be formed in the bandgap of semiconductors when a core hole and an electron pair up. For example, if the $2p$ level is excited in silicon, an exciton is formed that has a binding energy of about 0.9 eV that places it in the gap. It shows up in the photoabsorption spectra.

IMAGING MICROSCOPES

Imaging X-ray microscopes are somewhat similar in optical design to traditional visible-light microscopes in that an im-

age of an object is formed solely with the aid of lenses operating on the detector side. Depending on the detection method, these instruments operate in either (X-ray) transmission or (electron) emission mode. Both types will be described below. Some use specialized X-ray optics, whereas others use electron optics to image the sample.

Transmission

The sample is illuminated with X rays at the region of interest, and the transmitted X rays are used to produce a magnified image of the sample. An example of such an instrument is that developed by Meyer-Ilse at the Advanced Light Source (ALS) of the Lawrence Berkeley National Laboratory (LBNL) (8). Shown in Fig. 3, it uses a condensing Fresnel zone plate (FZP), a diffractive optic similar to a circular diffraction grating whose pitch increased with radial distance from the center. This condensing FZP focuses the X rays onto a 15 μm pinhole, after which they emerge from vacuum into a small space filled with helium gas, where the sample is mounted. Helium is used instead of air or another gas because it has low absorption in the X-ray regime. The X rays pass through the samples (which are typically cells, tissues, or microorganisms encased in a SiNH window in their growing solution), where they are scattered, and then enter another vacuum chamber, where an objective FZP forms an enlarged image of the sample and projects it onto a CCD camera. This instrument has demonstrated a resolution of 43 nm (9). A similar X-ray microscope at the Aarhus electron storage ring in Denmark has been used to study systems as diverse as human spermatozoa at various stages of maturation and iron-precipitating bacteria used for water treatment (10).

Emission

Emission mode microscopes directly image the electrons (primary, secondary, or Auger electrons) ejected from the sample to produce a magnified image of it. The photon energy can be varied to take advantage of variations in the absorption spectra of materials. The incident X rays are coarsely focused onto the sample, chiefly to uniformly illuminate the region of interest and to minimize flux loss and its resultant degradation of the signal-to-noise ratio. The spatial resolution is limited by the electron optics and inherent aberrations.

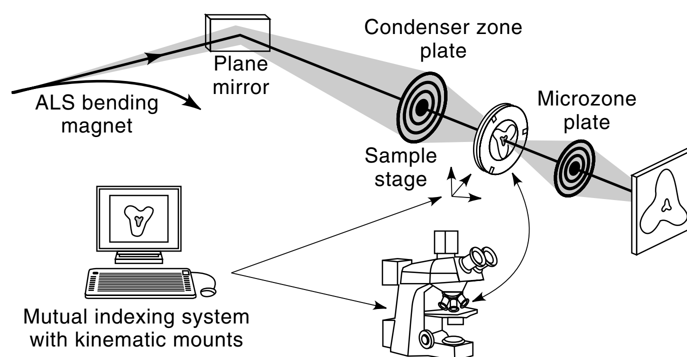

Figure 3. Schematic of the XM-1 transmission X-ray microscope at the ALS of LBNL. (Courtesy of W. Meyer-Ilse.)

Two imaging photoelectron microscopes will be discussed below. One uses electrostatic optics, and the other uses electromagnetic optics.

Photoemission Electron Microscope. The photoemission electron microscope (PEEM) uses electrostatic lenses to form an image of the sample with photoelectrons. An immersion lens is used as an objective to focus the electrons. Typically, it consists of a primary electrode at high voltage to accelerate the electrons, and a three-electrode lens that forms a real image. The sample itself serves as the cathode. The real image can then be magnified further using an intermediate objective lens. Next, it can be projected onto an assembly of a microchannel plate (MCP) and a phosphor screen, using a projector lens made up of another three-electrode lens and a two-stage decelerating lens designed to lower the kinetic energy of the electrons to the sensitivity range of the MCP (11,12).

The resolution of the objective lens is approximated by

$$\delta = \epsilon K_0/|E| \tag{10}$$

where K_0 is the mean photoelectron kinetic energy and E is the electric field at the sample surface, and ϵ is a dimensionless constant of order unity (13). A typical resolution for a traditional PEEM (UV-PEEM) is several micrometers, but a resolution of 0.9 μm has been achieved (14). With very soft X rays, a resolution of 10 nm has been obtained using very low-kinetic-energy electrons (15). The theoretical total resolution is limited by chromatic aberration (since photoelectrons of different energies are focused at different positions) and residual spherical aberration in the objective lens itself, as well as by the aberrations arising from the high accelerating potential between the sample and the objective lens (16).

Improvements in the electron optics design can overcome some of these limitations. For example, a large accelerating potential of $\approx$20 kV can be used to decrease the angular spread of the photoelectrons, and to thus reduce the spherical aberration (which is proportional to the cube of the spread angle) and improve the resolution (17). The insertion of an aperture at the back focal plane of the objective lens also reduces chromatic aberration by blocking electrons that would not be focused exactly at the image plane. Smaller apertures improve spatial resolution more than larger apertures, but also reduce the signal level. Using a 20 μm aperture, De Stasio and coworkers have demonstrated a 50 nm resolution using the Raleigh criterion on a knife-edge (12% to 88% of full intensity) with their microscope MEPHISTO (18), which is shown in Fig. 4. This resolution is being improved by several microscopy groups even as this article is being written. It is also possible to add an energy-filtering detector to further reduce the chromatic aberration and to allow the extraction of more spectroscopic information by implementing photoelectron energy selection and analysis. In the case of the instrument PRISM, this was done by inserting an electrostatic “prism” energy filter between the intermediate and projector lenses. This “prism” consists of a sector of a hemispherical capacitor used in conjunction with circular apertures and coupling lenses at the input and output of the capacitor. The lenses preserve the image, and the capacitor behaves as a spherical mirror analyzer to provide the bandpass electron energy filtering. The ability to select the photoelectron energy also makes possible the acquisition of photoelectron energy

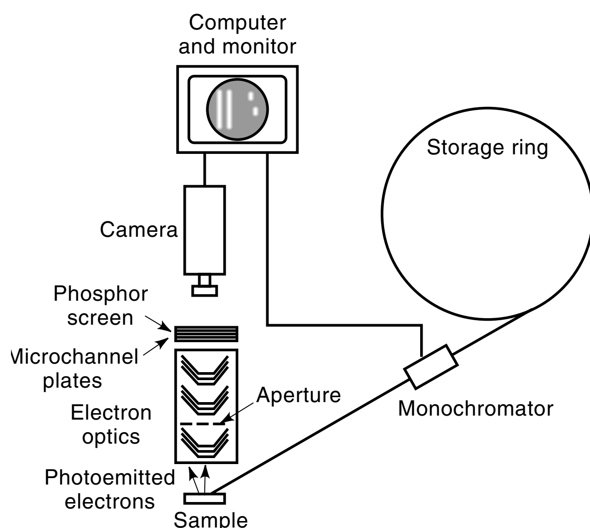

Figure 4. Schematic of the MEPHISTO photoemission electron microscope. (Courtesy of G. De Stasio.)

distribution curves (EDCs). PRISM has achieved a spatial resolution of 0.6 μm in energy-filtering mode on a 25 μm pitch gold grid; the Au 4*f* core level could be measured with an energy resolution of 1.0 eV and was used for chemical imaging. Currently, PRISM is operating without the energy filter, that is, as a standard X-ray PEEM (X-PEEM). To date, PRISM has achieved a resolution of 0.25 μm in X-PEEM mode (19).

PRISM in X-PEEM mode was used to study the formation of titanium silicide ($TiSi_2$) in a patterned sample with microstructures ranging from 100 μm to 0.1 μm. $TiSi_2$ is an important material used for interconnects in ultra large-scale integration (ULSI) devices. It occurs in two phases: the high-resistivity (60 $\mu\Omega \cdot$ cm to 90 $\mu\Omega \cdot$ cm) metastable C49 phase, and the desirable low-resistivity (12 $\mu\Omega \cdot$ cm to 15 $\mu\Omega \cdot$ cm) stable C54 phase, into which C49 is transformed with higher-temperature annealing. The formation of C54 is, however, inhibited for submicron lines, leading to a rise in resistivity. This poses a problem since $TiSi_2$ is used to reduce contact resistance in modern MOS (metal oxide semiconductor) devices, which are now being fabricated with sub 0.25 μm linewidths. Since the trend is to shrink linewidths (and, hence, devices) even further, the inhibition of the formation of the low resistivity phase of $TiSi_2$ at small linewidths is an important issue.

C54 has a face-centered orthorhombic crystal structure, while C49 has a body-centered orthorhombic crystal structure with different lattice constants. This leads to different bonding between Ti and Si in the two phases, and hence we should expect the chemical shift between core electron binding energies in C49 and C54 to be reflected in different photoelectron spectra. As seen in Fig. 5, photoelectron images acquired on the Ti $L_{2,3}$ absorption edge show dramatic differences at different photon energies, with the spoke tips and edges appearing brighter than the spoke centers at a photon energy of 455 eV. This suggests a local difference in chemical status of titanium silicide. In fact, absorption spectra taken on regions 1–4 as defined in Fig. 6(b) show that spectra acquired on a spoke tip and a spoke edge (regions 2 and 3) have a higher intensity in the 454 eV to 457 eV energy range than the spectra acquired on blanket silicide or on a spoke center (regions 1 and 4). (See Fig. 7.) This difference is consistent with C54 $TiSi_2$ being formed in spoke centers and C49 $TiSi_2$ remaining untransformed not only at spoke tips but also at spoke edges (20,21). This was the first successful application of spectromicroscopy to the study of $TiSi_2$ formation and revealed that C54 formation is inhibited not only in small features but at feature edges as well, suggesting a dependence on geometry that has been borne out by other experiments (22).

Other experiments facilitated by PEEM include mapping of domains on magnetic recording disks using magnetic circu-

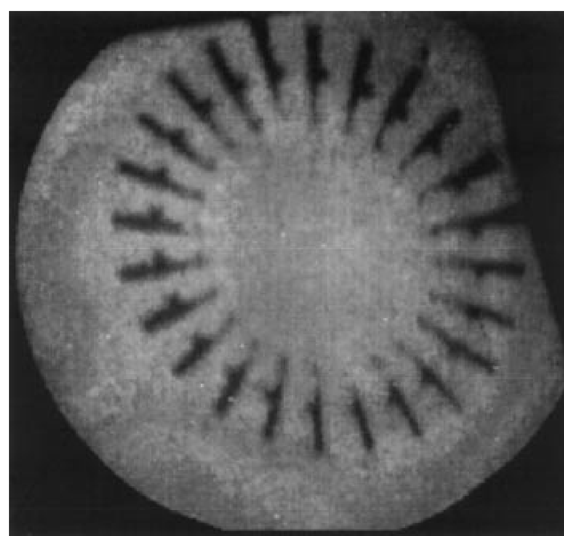

(a)

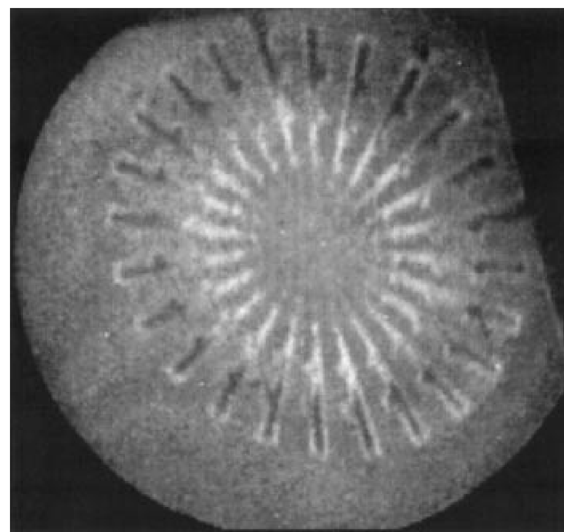

(b)

Figure 5. Photoelectron images of silicided-Ti-on-Si resolution test pattern. In (a), acquired below the Ti $L_{2,3}$ edge at 445.5 eV, only the centers of the spokes show up, and these are dark (absorbing). In (b), acquired at 455 eV on a shoulder on the edge, the spoke tips and edges emit much more strongly than the spoke centers, indicating a change in bonding.

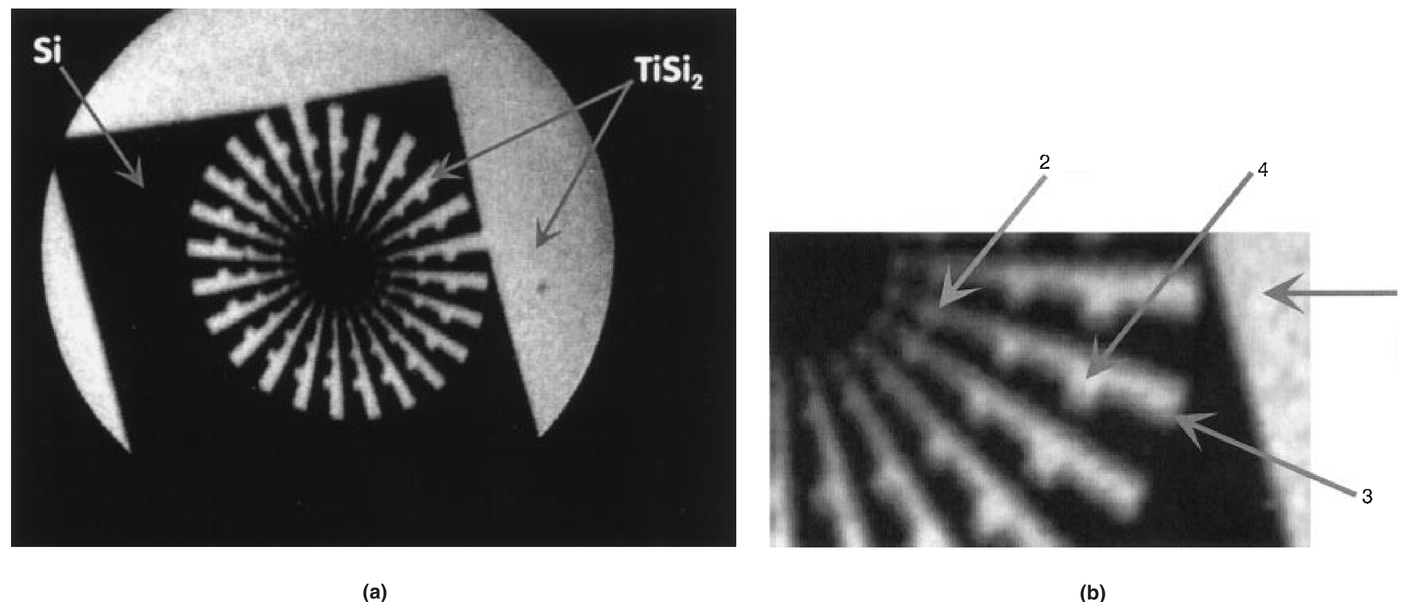

Figure 6. Photoelectron image of silicided STAR acquired at 464 eV. The width of the entire spoke pattern in (a) is 80 μm, and the spoke width at the points where it touches the edge of the square is 5 μm. A magnified view is shown in (b), where region 1 is on a blanket $TiSi_2$ area outside the pattern, 2 is on a spoke tip, 3 is on a spoke edge, and 4 is in the center of a spoke.

lar X-ray dichroism (MCXD) (23,24) and spatial and temporal waves of oxidizing CO on platinum (25,26).

Magnetic Imaging Photoelectron Microscope. The MicroESCA manufactured by Surface Science Instruments is a commercial version of this type of X-ray microscope.

A superconducting (typically NbTi) solenoid is used to bathe the sample in a uniform magnetic field that diverges from the sample normal. The photoemitted electrons spiral about the diverging magnetic field lines and are projected on a resistive anode detector to form an image magnified by a factor of about 70. A supplementary magnification or demagnification is attained by using two field coils around the detector to modify the solenoid's magnetic field near the detector. This feature results in a possible magnification ranging from 20× to 140×. An electron-retarding-grid energy analyzer placed before the detector acts as a high-pass filter and allows the acquisition of photoelectron spectra. Because the electrons are collimated along the field lines, there is little loss of signal at the analyzer as long as it intercepts enough of the field. This collimation results in the additional benefit of a high (0.1 eV) energy resolution for 100 eV photoelectrons. Such a resolution is well suited to the detection of subtle chemical shifts (27).

The spatial resolution is proportional to the radius of the helical path traveled by the electrons. For off-axis photoelec-

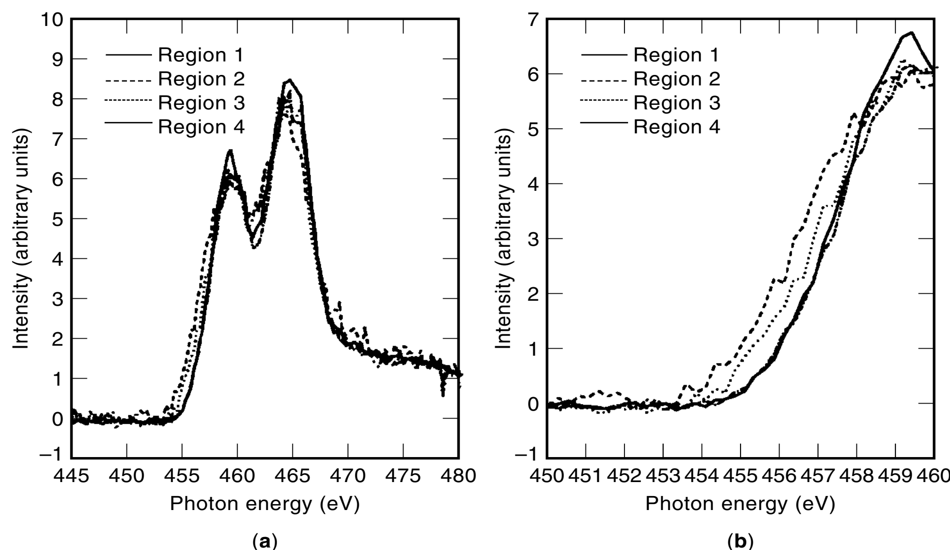

Figure 7. Ti $L_{2,3}$ absorption spectra acquired on regions 1–4 as defined in Fig. 6(b) are shown in (a). A closeup of the Ti L_3 edge in (b) shows that the tips (as in region 2) and the edges (as in region 3) have a higher intensity in the range between 454 eV and 457 eV that is not present in the blanket silicide or at the centers of the spokes, suggesting a difference in bonding in narrow features and feature edges.

trons, this is the cyclotron radius:

$$R_{\max} = (2mE_0)^{1/2}/eB_0 \tag{11}$$

where E_0 is the photoelectron kinetic energy and B_0 is the magnetic field strength at the sample. B_0 can range up to 8 T. The spatial resolution is estimated to range between $0.1R_{\max}$ and $2R_{\max}$. For electrons of kinetic energies from 10 eV to 1000 eV, the practical resolution ranges from 3 μm to 30 μm (28,29).

The commercial MicroESCA has seen various applications, ranging from geological samples to heterostructures. One experiment with Au/GaAs showed variations in the surface segregation of As as a function of gold distribution (29). One of the original research instruments is currently operating at the Synchrotron Radiation Center (SRC) of the University of Wisconsin—Madison and has been used for spectromicroscopic study of spatial variation in the oxidation of Bi in a high-T_c Bi–Sr–Ca–CuO superconductor (30).

SCANNING MICROSCOPES

Scanning X-ray microscopes finely focus the X rays to a micrometer- to submicrometer-sized spot on the sample. This spot is then rastered across the sample, with a signal collected for each (x, y) point. The scanning is most simply achieved by rastering the sample. The success of scanning X-ray microscopy is dependent on the quality and efficiency of the X-ray optics used for focusing the X rays to a point. Scanning X-ray microscopes exist in both transmission and emission flavors.

Transmission

The scanning transmission X-ray microscope (STXM) is the primary microscope of this type in existence. Developed by Schmahl (31) for use on the ACO ring in France, this type of microscope was also implemented by Kirz (32) at the NSLS of Brookhaven National Laboratory. It too uses a FZP to focus the X rays onto the sample, which is rastered using a scanning stage to obtain an image. The FZP was fabricated at IBM and has a focal length of 1 mm at a wavelength of 3.6 nm. Using the Raleigh criterion discussed below under "Diffraction-Limited Optical System," the resolution δ of the first order (which is the most intense) is given by

$$\delta = 1.22\,\Delta r \tag{12}$$

where Δr is the width of the outermost zone of the FZP. A central stop is used to block higher diffraction orders, and a pinhole is placed between the FZP and the sample to eliminate unfocused light. A wire proportional counter is used to measure the transmitted X-ray signal. The instrument operates in an atmosphere of helium (33). Biological studies, including those of live and wet specimens, are the primary application of this microscope, as they are for Meyer–Ilse's imaging microscope described above in the subsection "Photoemission."

Energies in the water window (between the carbon and oxygen K edges) are well suited because of the transparency of water and the absorbency of carbon (in biological structures) in this range. Several experiments on chromosomes have been done (32,34). The STXM was later applied to chemical imaging using NEXAFS signals of other systems such as diagonally sectioned Kevlar fibers, which exhibit linear dichroism (35). This instrument has also been used to study a polycarbonate–polyethyleneterephthalate (PC–PET) polymer blend. By varying the incident photon energy, it is possible to track an electronic resonance between carbonyl groups and the phenylene in the polymers. Figure 8 shows X-ray micrographs of the sample acquired at 284.8 eV and 285.1 eV (36). The contrast is reversed in the two images, with the PET bright and PC dark at 284.8 eV and the PC bright and PET dark at 285.1 eV. The shift in the NEXAFS microspectra shown in Fig. 9, which were acquired on both PC and PET areas of the sample is responsible for this contrast. The NSLS STXM has achieved submicrometer resolution. A newer instrument installed at the ALS has attained a resolution of 0.12 μm (37).

Emission

There are several advantages the scanning emission microscope has over the imaging emission microscope, including (1) the possibility of detecting transmitted X rays and luminescence signals in addition to photoelectron signals, (2) decoupling of the imaging mechanism from the signal collected, (3) a single optical element whose aberrations can be minimized, (4) a standard detector and its accompanying ease of obtaining spectra, and (5) a higher theoretical spatial resolution. Several different approaches will be discussed below.

Scanning Photoemission Microscope. The FZP-based design for the scanning photoemission microscope (SPEM) arose from the STXM discussed above in the subsection "Transmission." It is a UHV instrument and is typically operated in the energy range of 650 eV to 680 eV with a resolution of 2 eV in order to maximize flux at the sample. At these wavelengths (1.8 nm to 1.9 nm) the focal length is about 5 mm, but the pinhole needed to block unfocused light needs to be placed about three-fourths of the focal length away from the FZP before the sample. The working distance, therefore, is less than 1.5 mm, and part of the microscope must be placed in the cylindrical mirror analyzer (CMA) used for electron energy analysis. The CMA has been modified to accommodate the FZP, the pinhole, and a tilt assembly to align the two. Both the sample current and the CMA signal can be used to acquire images, and the CMA can be used to obtain EDCs as well. This instrument has reached submicrometer resolution and has been used in test experiments on a commercial device at the NSLS (38). A SPEM, which achieves scanning by moving the zone plate instead of the sample stage, thus facilitating in situ sample treatment such as heating or cooling, is operational at the ALS (68).

Another SPEM is already working at the third-generation ring in Trieste in the energy range of 300 eV to 400 eV. This microscope has submicrometer resolution and is being used for surface studies of metals and semiconductors (39). A high-energy SPEM is in place at the Advanced Photon Source (APS) of Argonne National Laboratory. It uses blazed phase-shifting FZPs, which can theoretically achieve an efficiency of 80%, compared to 10% for ordinary FZPs (40). This microscope can focus hard X rays down to a 0.25 micrometer spot. This spot can then be scanned across the sample while collecting the X-ray fluorescence signal, thus obtaining a chemical

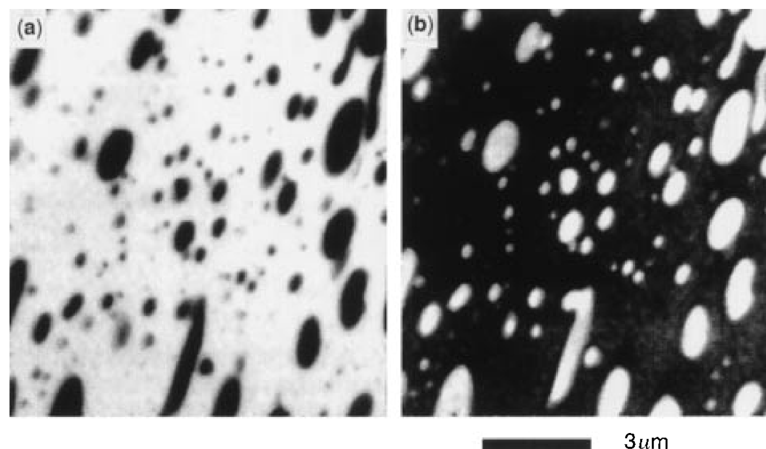

Figure 8. Transmission X-ray micrographs of a PC-PET polymer blend. (a) was acquired at a photon energy of 284.8 eV (energy *A*), and (b) at 285.1 eV (energy *B*). PET appears bright in (a), and PC in (b). (Courtesy of H. Ade.)

map of elements present in very dilute concentrations in the sample. Because of the high-energy X rays used, the experiments can be carried out in air. Biological samples such as plant roots from *Plantago* and *Arabidopsis* have been studied. The X-ray microprobe has also been used for strain measurements using microdiffraction techniques (41–43).

Hamburg Microscope. Designed by Christoph Kunz, this instrument uses a ring ellipsoid mirror to focus monochromatized X rays from wiggler radiation onto the sample. Unlike the FZP, the ellipsoid mirror's focal position is independent of the wavelength, allowing easy switching between wavelengths of interest without moving the sample or the optics to stay at the focus. Its efficiency is also higher because it operates at grazing incidence. In practice, the flux is limited because of problems in illuminating the mirror properly without loss. It is installed on the FLIPPER monochromator at HASYLAB of DESY, Hamburg. The source is situated at one focus of the ellipsoid, and the sample is placed at the other focus. A resolution of 0.4 μm has been achieved at 200 eV. The instrument can also operate at lower resolutions over the entire range of 20 eV to 1300 eV. Mirror quality is the obstacle in reaching higher resolutions. Since this is a grazing-incidence optical system, figure error is very important. The ellipsoidal mirror, custom manufactured by Carl Zeiss, is, like other aspheric mirrors, difficult to make. Because the tolerances for microscopy are so tight, this limitation becomes significant. Surface finish is important too, since surface roughness leads to scattering and hence loss of useful flux at the sample.

EDCs can be acquired with this instrument, as can photoelectron images at different energies. In addition, the total luminescence signal can be collected, thus allowing a luminescence image to be acquired simultaneously with a photoelectron image. This technique has been applied to the study of transition metal compounds, including variously doped LaOBr powders and chemical Tl^{1+}-doped CsI (3).

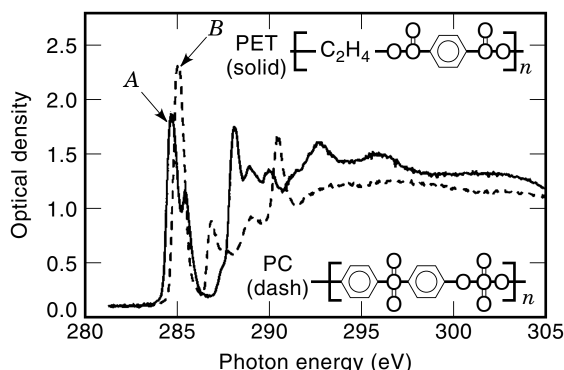

Figure 9. NEXAFS spectra from 0.1 μm^2 areas of PC and PET from a 70 : 30 PC : PET blend. PET and PC spectra have peaks at energies *A* and *B*, respectively. This explains the contrast observed in (a) and (b) of the previous figure. (Courtesy of H. Ade.)

Wolter Scanning Photoemission Microscope. The Wolter mirror is a glancing-optics objective consisting of an ellipsoidal section next to a section of a hyperboloid of revolution. The addition of the hyperboloid section corrects the aberrations of a single ellipsoid surface and increases the field of view. The application of these optics to X-ray microscopy was led by Hitachi, Ltd. and the University of Tsukuba, Japan. Like the ellipsoid mirror used in the Hamburg microscope, the Wolter mirror has a focus independent of the wavelength. It has less aberration than other grazing-incidence mirrors, but, since it too is aspheric, it also suffers from the same difficulties in accurate fabrication as the ellipsoid mirror, although the manufacturing techniques are different. (For the Wolter mirror, a vacuum replication process using epoxy resin and a precision-ground and -polished mandrel is used (44,45), whereas a direct grinding and polishing technique is used for Hamburg's ellipsoid.) The Wolter SPEM has been installed on a bending-magnet beamline at the Photon Factory synchrotron of the National Laboratory for High Energy Physics of Japan. Figure 10(a) shows details of the mirror design, while the actual experimental setup is depicted in Figure 10(b) (46). The mirror demagnifies the pinhole-defined source by a factor of 29.8. At a photon energy of 150 eV, the reflectivity is $\approx$77% for a Au-surfaced mirror, and the energy resolution is about 1 eV (47). The microscope has demonstrated a 0.3 μm resolution in total photoyield mode (in which all of the photoelectrons emitted are collected with the microchannel plate) and 2.0 μm in energy-selected mode (when a single electron energy is selected by the electron energy analyzer) (48). The latter value can be greatly improved by increasing the signal-to-noise ratio by operating with higher X-ray flux on an undu-

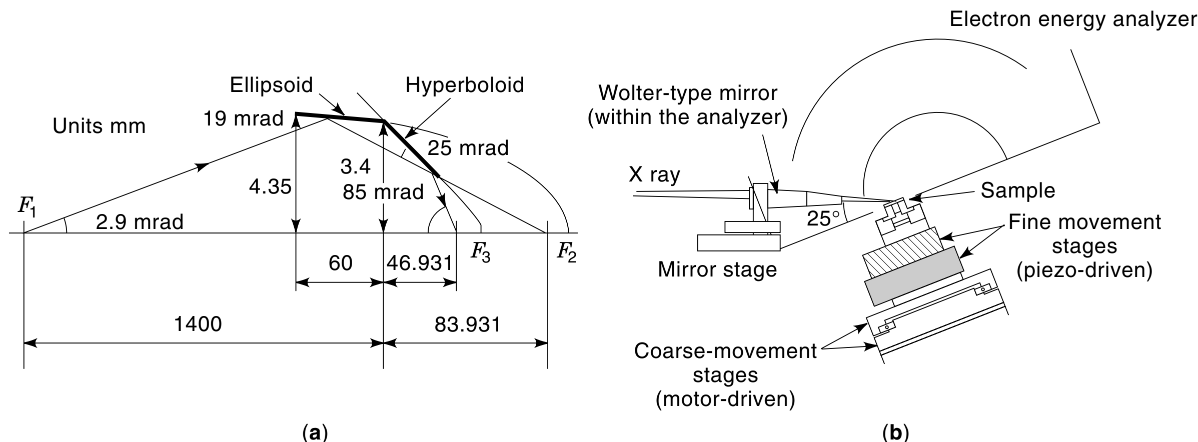

Figure 10. (a) Specifications of Wolter optics. (b) Layout of Wolter microscope developed by Hitachi. [Courtesy of M. Hasegawa (46).]

lator beamline. The relationship between the signal-to-noise ratio and resolution is discussed below in the subsection "Resolution: Limiting Factors."

Schwarzschild Objective. The Schwarzschild objective (SO) was described by Schwarzschild in 1905 and has been used in telescopes for a long time, but was applied to X-ray microscopy only some 20 years ago by Haelbich (49), following the suggestion of Eberhard Spiller that multilayers could be used as high-energy reflectors. A commercial SO from Ealing was coated with some of the first X-ray multilayers with sufficiently high reflectivity in normal incidence. The first synchrotron-based microscope using these optics was constructed at DESY's HASYLAB. The resolution at a photon energy of 62 eV was 1.5 μm, 25 times the diffraction limit. This was due to the poor alignment tolerances of the Schwarzschild objective used (49). Lovas, Spiller, and coworkers built a modified instrument with a SO designed to minimize aberration (comatic aberration in particular) and make diffraction-limited performance attainable. They forecasted a resolution of 0.1 μm in 1981 (50).

This did not prove so simple, however, and MAXIMUM, a soft-X-ray spectromicroscope developed at the University of Wisconsin—Madison, was the first and only such SO-based instrument to reach that resolution, more than a decade later (51). The design optical setup and design parameters of the SO used in MAXIMUM are shown in Fig. 11 and Table 1, respectively. Photographs of the mirrors coated with Ru/B_4C multilayers for a peak reflectivity at 130 eV are shown in Fig. 12. As shown schematically in Fig. 13, X rays emitted by an undulator are monochromatized to 130 eV and focused on a pinhole. The pinhole defines a source that is demagnified 20 times to form an X-ray microspot on the sample. The sample is scanned using a piezo-driven flexural hinge stage, and the photoemitted electrons are detected by an electron energy analyzer (a cylindrical mirror analyzer or CMA) to produce a two-dimensional photoelectron image. In another mode of operation, the sample is held fixed, and the CMA is used to collect an EDC of the photoelectrons.

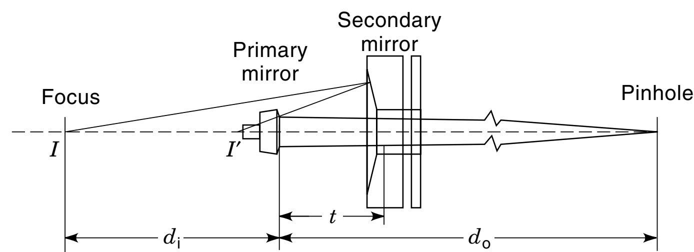

Figure 11. SO geometry and image formation.

In a $TiSi_2$ formation study done with MAXIMUM on beamline 6.3.2 of the Advanced Light Source of the Lawrence Berkeley National Laboratory, static random access memory (SRAM) wafers from IBM, East Fishkill, were subjected to Ti deposition and rapid thermal anneal (RTA) steps in an ultrahigh-vacuum (UHV) chamber attached to the main microscope chamber. This was done to avoid exposure to air, which would cause surface contamination and oxidation, and allowed a clean photoemission signal to be obtained from the $TiSi_2$ formed. $TiSi_2$ was expected to form on top of polysilicon features overlying a silicon dioxide base layer. The polysilicon pads and lines of the SRAM sample were silicided by depositing ≈30 nm Ti *in situ* after subjecting the wafer to a light chemical clean, then annealing at ≈800°C for 20 s and flashing to ≈1000°C. Figure 14(a) and (b) show two 100 μm × 100 μm photoelectron micrographs acquired at 25.74 eV and 20.48

Table 1. Design Parameters of Schwarzschild Objective

Object distance d_o	1298 mm
Image distance d_i	120.78 mm
Distance between mirrors, t	55.498 mm
Primary mirror:	
Radius of curvature	66.336 mm
Outer diameter	25.5 mm
Inner diameter	12.5 mm
Secondary mirror:	
Radius of curvature	117.253 mm
Outer diameter	80 mm
Inner diameter	25.5 mm
Demagnification	20×
Numerical aperture	0.2

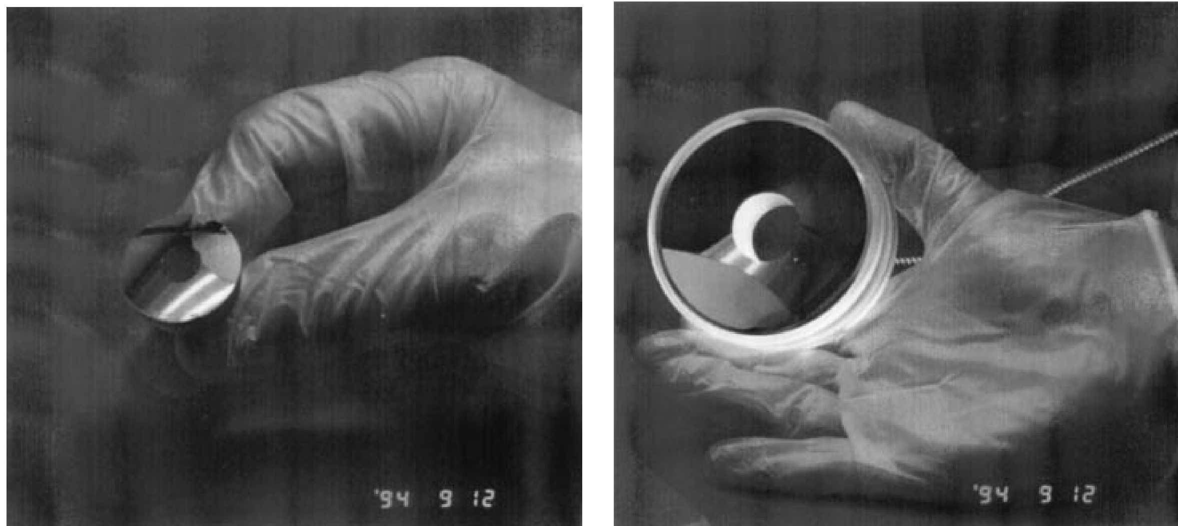

Figure 12. Primary and secondary mirrors of the Schwarzschild objective coated with Ru/B_4C multilayers. Note the pinholes in the coating that alllow light through.

eV, respectively, of the same area of a SRAM sample. These energies correspond in turn to the unshifted and oxide-shifted, respectively, Si 2*p* core levels shown in the EDCs in Fig. 14(c). The two EDCs were taken on a pad (region A) and on an area near the pad edge (region B) that appears bright in Fig. 14(b). The photon energy was 129.3 eV.

The lines and pads appear to be unaffected in Fig. 14(a), but exhibit a different morphology in Fig. 14(b). Images acquired with secondary photoelectrons were similar to Fig. 14(b) as well. However, secondary-electron images taken *before* the (unusually high) formation anneal resembled Fig. 14(a), as did images taken on samples silicided with the normal 700°C to 900°C sequence. This suggests that the differences observed in Fig. 14 and are due to the high-temperature processing, namely the resulting agglomeration of the silicide in the lines and also lateral growth of the $TiSi_2$ onto the SiO_2 at the edges of the silicided polysilicon regions. Because Fig. 14(b) is tuned to the SiO_2 signal, we can conclude that the bright regions in this image represent a larger amount of SiO_2 at the surface. This is because some regions of the SiO_2 are exposed by agglomeration of the overlying laterally grown $TiSi_2$. The laterally grown silicide is also thinner on the SiO_2 than the main silicide formed on the polysilicon,

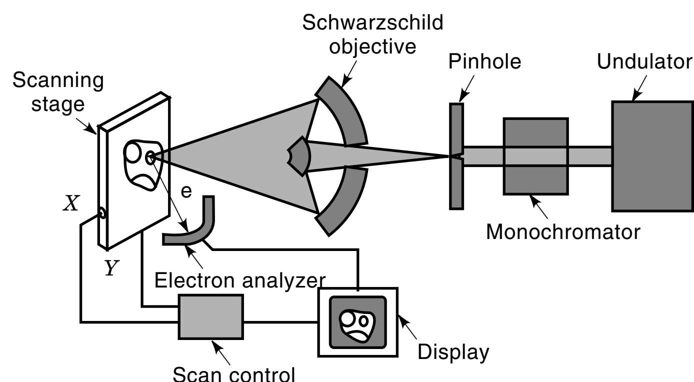

Figure 13. Schematic of the spectromicroscope MAXIMUM.

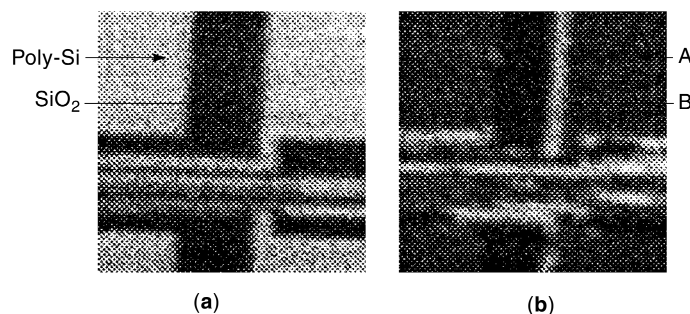

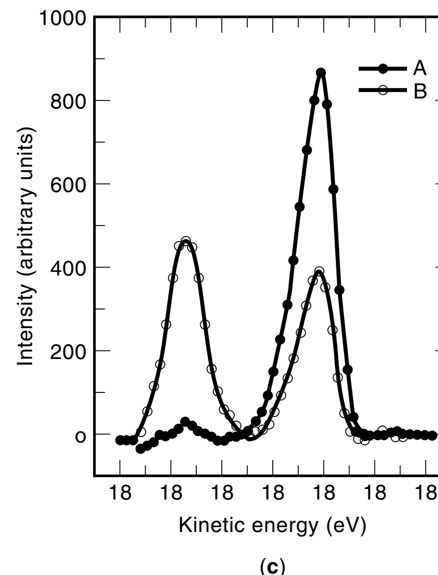

Figure 14. 100 μm × 100 μm, 1 μm step photoelectron maps of the same silicided area taken at the unshifted (25.75 eV) and oxide-shifted (20.48 eV) peaks of the Si 2*p* core level shown in the EDC.

whence the higher oxide signal there. Neither effect is evident in Fig. 14(a), which is tuned to the unshifted Si 2*p* because the Si concentration is always higher in the main silicide formed on the polysilicon than on the Ti-covered silicon oxide or the thin laterally grown silicide. SEM analysis showed a similar morphology to that observed in Fig. 14(b), reflecting the differences in emissive characteristics of the materials and corroborating the presence of agglomeration.

MAXIMUM has also been applied to the study of another type of interconnect used in the semiconductor industry: Al–Cu alloy. Electromigration in interconnect lines is the transport of material along with electron flow when a current is passed through the line. This can lead to the formation of voids and, eventually, an open circuit. It is a complex and important phenomenon that is described in detail in the article ELECTROMIGRATION of this Encyclopedia. The presence of Cu is thought to retard the electromigration process. Cu is, however, not very soluble in Al and hence may segregate to different phases such as θ-Al_2Cu as well as to different locations in the line such as grain surfaces and interfaces.

A 5 μm wide line patterned in a 4% Cu Al–Cu alloy on thermal oxide grown on Si was stressed (by passing current and heating *in situ* in the microscope chamber) to induce electromigration. The line was examined with MAXIMUM before and after electromigration. Images acquired at different photoelectron energies before and after stressing are shown in Fig. 15. Already before electromigration, the image acquired at 122 eV (the Cu 3*d* core level) shows bright spots corresponding to Cu-rich precipitates. A comparison between spectra acquired on the precipitate labeled P and a uniform, "ordinary" area O is shown in Fig. 16(a). P exhibits a stronger Cu 3*d* signal than O, as expected, in Fig. 16(a). The presence of Cu in the Al film at P shifts the Al 2*p* core level to lower binding energy (higher kinetic energy) with respect to O, as can be seen in Fig. 16(b). This explains why the image in Fig. 15(a), acquired using 50 eV photoelectrons, shows the precipitates brighter than the uniform film area, while that acquired using 47 eV photoelectrons shows them darker. The chemical shift to higher kinetic energy results in more emission from the precipitates at 50 eV and more from the O area at 47 eV.

After electromigration, it is seen from Fig. 15(b) that the Cu-containing precipitates have not moved and that voids have formed in the line. The void areas in the photoelectron image acquired at 42 eV appear bright because of surface charging of an Al_2O_3 skin left behind over the void. This charging causes the Al 2*p* core level to be shifted to higher binding energies (since the sample becomes positively charged during photoemission because the void prevents a good earth connection to supply electrons, thus causing electrons to be more tightly bound) and hence lower kinetic energies, resulting in the void appearing bright at the shifted Al 2*p* peak at 42 eV (69).

There are other implementations of the SO microscope as well. Another microscope has been designed to run the SO with C $K\alpha$ radiation (277 eV). This relatively high energy (for normal-incidence optics) is made possible by the use of NiCr/C multilayers. The objective's resolution has been measured to be better than 0.5 μm (52).

IMAGE FORMATION

So far we have discussed many different approaches to X-ray microscopy and have compared the resolutions achieved and have listed experiments performed, but we have not yet done a detailed analysis of the image formation itself. We will do so here for microscopes utilizing X-ray optics and synchrotron radiation.

Synchrotron radiation can be generated by three types of devices: bending magnet, wiggler, and undulator. The first two types are similar in their broad energy spectrum and their large opening angles of radiation and can be treated together. In both a bending magnet and a wiggler, the radiation from one electron at one point is independent of that at a different point in the synchrotron, and photons are emitted incoherently along the tangent at each point of the electron trajectory. However, when the emittance of the electron beam becomes very small (as it does for third-generation synchrotron sources such as the ALS), diffraction effects arise along the electron trajectories (53). The interference effect is very strong in undulators because of the small opening angle of the radiation and results in a spectrum with harmonic peaks at certain wavelengths. This spectral purity implies a high degree of inherent temporal coherence in undulator radiation, unlike bending-magnet and wiggler radiation. The photon field and the trajectory remain in phase over a large distance. Again, when the emittance of the electron beam is very small, the radiation cannot be assumed to be spatially incoherent.

It is convenient to define the following phase-space relationship for quasimonochromatic sources such as undulators:

$$d \cdot \theta \geq \lambda/2\pi \tag{13}$$

where d is the source (electron beam) diameter, and θ is half the opening angle of the radiation, which is determined solely by the electron trajectory. If the source has an opening angle θ at a wavelength λ, any points separated by less than $\delta = \lambda/\sin\theta \approx \lambda/\theta$ cannot be resolved, that is, the source is *spatially coherent,* or *diffraction-limited.* The source size d is larger than δ in practice, however. Currently the ALS has undulators with a phase-space at least 5 to 50 times larger than the diffraction limit (54).

As stated earlier, even the radiation from bending magnets and wigglers has some spatial coherence and, although not temporally coherent, is typically monochromatized before entering the X-ray imaging system. Thus we can speak in general of the quasimonochromatic synchrotron radiation used in X-ray microscopes as being *partially coherent.*

The Frequency Response of an Optical System

Spatial-Frequency Cutoff. Following the treatment of Born and Wolf (55), let us consider the two limiting cases of coherent and incoherent illumination. $\mathcal{K}$, the *frequency response function* in the coherent case, is actually equivalent to the pupil function G with a change of variables, and we may write

$$\mathcal{K}(f, g) = G(\lambda R f, \lambda R g) \tag{14}$$

where R is the radius of the Gaussian sphere of reference (which is centered on the geometric image point and passes through the center of the exit pupil). Because the pupil function has a value of zero outside the exit pupil itself, frequencies above a certain value are not transmitted. In particular, if the exit pupil is approximated by a circle of radius a, then the pupil function will be zero for points outside the circle and

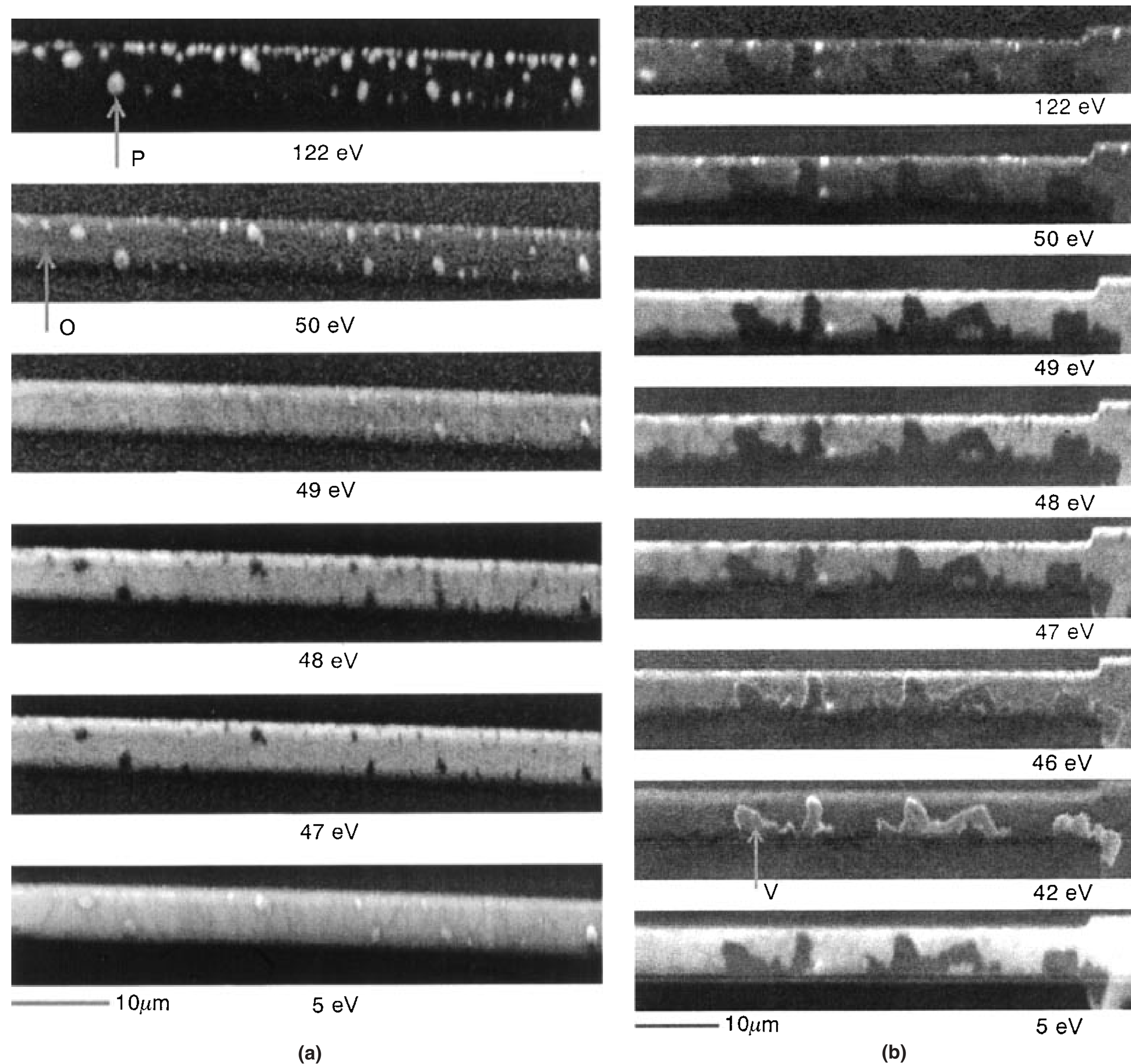

Figure 15. (a) Micrographs of 5 μm wide Al–4% Cu line before electromigration. P labels a Cu-containing precipitate, and O labels an "ordinary" point on the line. (b) Micrographs of 5 μm wide Al–4% Cu line after electromigration. V marks a void. Images are acquired at the indicated photoelectron energies. (Courtesy of M. Solak.)

only those frequencies will be transmitted for which

$$(\lambda Rf)^2 + (\lambda Rg)^2 < a^2 \tag{15}$$

holds. For an optical system with a small image-side angular aperture that obeys the sine condition

$$M = \frac{y_1}{y_0} = \frac{n_0 \sin\theta_0}{\eta_1 \sin\theta_1} \tag{16}$$

where M is the magnification and n_0 and n_1 the indices of refraction in the object and image spaces, respectively—we may make the approximation

$$\frac{a}{R} = \tan\theta_1 \approx \sin\theta_1 \tag{17}$$

where θ_1 is the half angle. For a one-dimensional (1-D) object, if $\Delta y_0 = 1/g$ is the period corresponding to the spatial frequency g, we may write that only those frequencies corresponding to the spatial periods that satisfy

$$P_y > \frac{\lambda_0}{A_1} \tag{18}$$

where $\lambda_0 = n_1\lambda$ is the vacuum wavelength and $A_1 = n_1 \sin\theta_1$ is the image-side numerical aperture, are transmitted.

In the incoherent case, $\mathscr{L}$ is the frequency response function and, because of the connection between $\mathscr{K}$ and the pupil function G shown in Eq. (14), is also the autocorrelation function of the pupil function. If we again consider a circular exit pupil of radius a, the autocorrelation function will have a non-

zero value only if there is some overlap between two displaced pupil functions, for example, if the maximum displacement between the two pupil functions is less than the pupil diameter $2a$. Thus only those frequencies will be transmitted that satisfy

$$(\lambda Rf)^2 + (\lambda Rg)^2 < (2a)^2 \tag{19}$$

Then, for a 1-D object, only those spatial frequencies will be transmitted whose spatial periods satisfy

$$P_y > \frac{\lambda_0}{2A_1} \tag{20}$$

The spatial frequency cutoff for the partially coherent case falls between the cutoffs for the coherent and incoherent cases. In general, the minimum spatial period resolvable, Δ, is the reciprocal of the cutoff frequency. For

$$\Delta = d\frac{\lambda_0}{A_1} \tag{21}$$

we have

$$\begin{aligned} d &= 1 && \text{coherent} \\ d &= \tfrac{1}{2} && \text{incoherent} \\ \tfrac{1}{2} < d &< 1 && \text{partially coherent} \end{aligned} \tag{22}$$

Accordingly, incoherent illumination can resolve the smallest spatial period, and hence can produce the highest spatial resolution, followed by partially coherent, and then by coherent illumination. It is important to note, however, that the results obtained here apply rigorously only for an unobstructed circular exit pupil in an optical system that has a small angular aperture and satisfies the sine condition. Other pupil illumination functions may increase or decrease the resolution.

Diffraction-Limited Optical System. All axially symmetric X-ray scanning systems (e.g., SO-based microscopes, the SPEM, and the STXM) have a central obstruction. All microscopes, both scanning and imaging, also have aberrations. These and other effects in real systems can be taken into account in the formulation of the complex transmission function K and are reflected in its inverse Fourier transform $\mathscr{K}$, which is directly related to the frequency response function in the coherent, incoherent, and partially coherent cases. We will not treat the complex topic of aberrations here. Rather, we will treat the opposite, ideal case of the *diffraction-limited optical system.*

The term "diffraction-limited" is often bandied about in X-ray microscopy. We have used it ourselves when talking about third-generation synchrotron sources, but it is different for photons. An imaging optical system is called diffraction-limited if it converts a spherical wave emanating from a point source into another spherical wave converging to the Gaussian image point in the imaging plane (56). If the wavefront leaving the exit pupil is not perfectly spherical, it is an indication of aberrations in the system. In a diffraction-limited system, then, only the functional form of K is important in determining the system's imaging properties. We consider an optical system of small enough angular aperture to justify the paraxial approximation and the lens equation

$$\frac{1}{d_0} + \frac{1}{d_1} = \frac{1}{F} \tag{23}$$

where d_0 is the object distance, d_1 is the image distance, and F is the focal length of the lens.

For such a system and coherent illumination, the complex transmission function K is given by the Fraunhofer diffraction pattern of the lens aperture centered on the geometrical image point (56). Then for a lens with a circular aperture and a central circular obstruction we may write

$$K(x, y) = \frac{1}{1-\epsilon}\left(\frac{J_1(\nu)}{\nu} - \frac{\epsilon J_1(\epsilon\nu)}{\nu}\right) \tag{24}$$

where J_1 is a Bessel function of the first order, $\nu = 2\pi\sqrt{x^2 + y^2}$, with x, y measured in units of λ/A_1, and ϵ represents the fraction of aperture obstructed and ranges from 0 to 1. It can be seen that if $\epsilon = 0$ Eq. (24) reduces to the Fraunhofer diffraction pattern from a circular aperture. $K(x, y)$ is also called the amplitude point spread function and is the impulse response of the optical system. [$\mathscr{K}(f, g)$, the inverse Fourier transform of $K(x, y)$, is the frequency response of the system, as stated earlier.]

For incoherent illumination, the frequency response of the system is $\mathscr{L}(f, g)$, and the impulse response (also called the

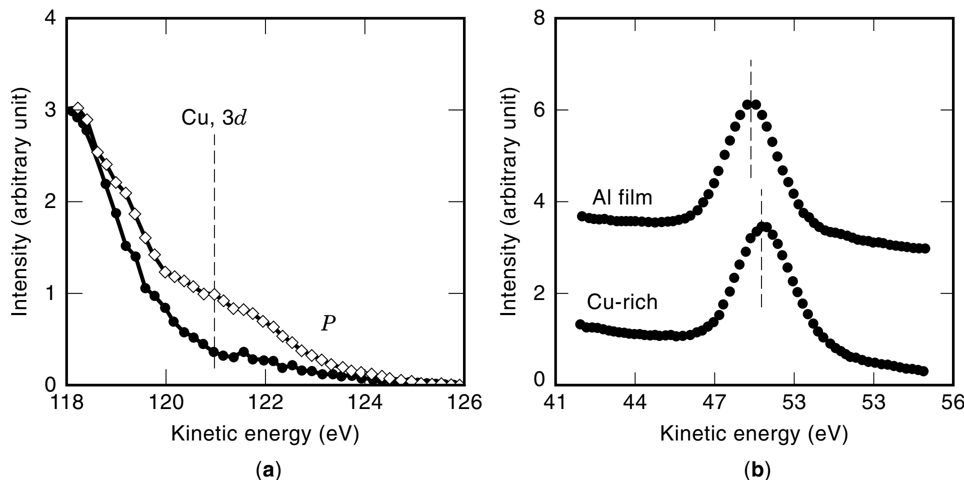

Figure 16. (a) EDCs acquired at points P (precipitate) and O (ordinary) of Fig. 15(a) showing higher Cu 3*d* signal at P. (b) EDCs acquired on an Al film area O and a Cu-rich area P, showing that the presence of Cu shifts the Al 2*p* to higher kinetic energy (lower binding energy). (Courtesy of M. Solak.)

intensity point spread function) is given, for an annular aperture, by the square of K as defined in Eq. (24). For a circular aperture, $\epsilon = 0$ and the impulse response is the Airy pattern.

Scanning emission microscopes like MAXIMUM are *incoherent* imaging systems in that, even though the illumination may be partially coherent, the photoelectron signal collected per pixel has no relation to the phase of the incident light and hence is incoherent with that of neighboring pixels.

What is the Meaning of Resolution?

There are several criteria than can be used to determine the resolution of an imaging optical system. One commonly used criterion is the Rayleigh criterion. Strictly speaking, it applies only to an aberration-free, unobstructed optical system. According to this treatment, two monochromatic and mutually incoherent point sources can just barely be resolved if their separation is such that the maximum of the Airy pattern of one point falls on the first minimum of the other's Airy pattern, resulting in a saddle point between the two maxima of the summed pattern. This separation δ is given by

$$\delta = \frac{1.22\lambda}{2A_1} \tag{25}$$

and is also the diameter of the Airy disk. For a scanning microscope, the two point sources are replaced by two small pinholes with a diameter much smaller than their separation, but the same analysis applies. Often, δ is quoted for a microscope although the preconditions of incoherence and lack of aberration may not be satisfied. This is permissible only as an approximation. In addition, strictly speaking, $\lambda/2A_1$ is the diffraction-limited resolution of an *incoherent* imaging system. (λ/A_1 is the diffraction-limited resolution of a *coherent* imaging system.) However, since this is close to the Rayleigh criterion [Eq. (25)], the two terms are sometimes used interchangeably, and the factor of 1.22 crops up.

Although, the diffraction-limited resolution has long been thought to be the ultimate resolution for an optical system, it is in principle possible to resolve certain types of objects that are smaller. Goodman (57) states two theorems that apply to bounded objects. The first theorem states that the Fourier transform of a function bounded in the (x, y) plane is an analytic function in the (f, g) plane. The second theorem states that if an analytic function in the (f, g) plane is known exactly in an arbitrarily small finite region, then the whole function can be found uniquely by analytic continuation. For an optical system and a bounded object, this means that the entire object frequency spectrum can be calculated by analytic continuation if a finite portion of it can be determined exactly (in the absence of noise) from the image frequency spectrum, which is determined by the frequencies passed by the point spread function of the optical system. Thus, because the entire object frequency spectrum is then known, the object itself can be reconstructed exactly, thus allowing a kind of *superresolution.* This may be possible, for instance, in the ubiquitous case of the circular aperture. If the surrounding material is not completely opaque to the incident light, but rather induces a phase shift, it is possible to narrow the diameter of the Airy disk. Since the diameter of the Airy disk is a good estimate of the resolution, this will improve the resolution too.

Actually, assuming that a finite portion of the object frequency spectrum is an analytic function is a highly restrictive hypothesis, since it is difficult to have a priori knowledge of the object. Normally we have an unknown object to which we apply criteria such as the Rayleigh criterion to determine the resolution. But in that case we have available only the information that is transmitted by the optical system, and not intrinsic information about the object. Thus it appears that the amount of information that can be transmitted by an optical system is fixed, and if the resolution is to be improved, it must be at the expense of something else. In theory superresolution should be feasible in some controlled cases, but in the real world there is significant noise, which limits the accuracy with which the frequency spectrum of the bounded object can be measured within the spatial-frequency bandpass of the optical system. This effect, together with the effect of aberrations, can preclude not only superresolution, but diffraction-limited resolution as well.

Resolution: Limiting Factors. Often the first question asked about a particular X-ray microscope is "What's its resolution?" The answer, once extracted, must include three values: the everyday resolution, the best resolution achieved, and the theoretical best resolution. The everyday resolution is the poorest of the three and arises from a compromise between spatial resolution, signal level, noise level, and other experimental parameters such as acquisition time and energy resolution. The best resolution is a much touted number and is typically obtained only with painstaking alignment and fine tuning followed by a lengthy data acquisition period. The theoretical best resolution depends on the image formation under different types of illumination, as discussed earlier. It is instructive to discuss the practical limitations on resolution in a quantitative way in order to understand and predict experimental results.

Effect of Noise. The signal measured in an image acquired with an X-ray spectromicroscope is a combination of the true signal and the background signal. The background signal can be a function of the photon energy or the photoelectron energy as well as of the spatial frequency. There is also noise accompanying both signals, and it reduces the image contrast. What is actually measured in the image is always intensity, regardless of the illumination. Thus we need to know the frequency spectrum of the intensity. For an incoherent system, which is linear in intensity, it is straightforwardly given by Eq. (26). For partially coherent and coherent systems, the intensity cannot be expressed in terms of a frequency transfer function acting as a linear filter to transform the object intensity $\mathscr{I}_0$ into the image intensity $\mathscr{I}_1$. As mentioned earlier, scanning emission microscopes are incoherent systems. Even transmission X-ray microscopes rely on the incoherence in partially coherent light to deliver higher resolution because of the higher spatial-frequency cutoff. It is useful, then, to examine the effect of noise in the mathematically simpler incoherent case:

$$\mathscr{I}_1(f, g) = \mathscr{I}_0(f, g)\mathscr{L}(f, g) \tag{26}$$

where $\mathscr{L}$ is the frequency response function for incoherent illumination. Another name for the normalized $\mathscr{L}(f, g)$ is the *optical transfer function* (OTF). The *modulation transfer func-*

tion (MTF) is simply $|\mathscr{L}(f, g)|$, the modulus of the OTF, and is a useful quantity for describing the resolving capability of an optical system under incoherent illumination. The MTF $\mathscr{T} = |\mathscr{L}(f, g)|/|\mathscr{L}(0, 0)|$ for the simple case of a diffraction-limited optical system with an unobstructed circular aperture can be obtained with K as in Eq. (24) and $\epsilon = 0$. Because of circular symmetry, radial coordinates may be used and the MTF may be computed to be

$$\mathscr{T}(f) = \begin{cases} 0, & f > f_0 \\ \dfrac{2}{\pi}\left[\cos^{-1}\left(\dfrac{f}{2f_0}\right) - \dfrac{f}{2f_0}\sqrt{1-\left(\dfrac{f}{2f_0}\right)^2}\right], & f \le f_0 \end{cases} \quad (27)$$

where f_0 is the incoherent cutoff spatial frequency $2A_1/\lambda$ (58). Using a linear approximation for the transmitted frequencies, we may write

$$\mathscr{T}(f) = 1 - \frac{f}{f_0} \quad (28)$$

and for a one-dimensional object we may rewrite Eq. (26) as

$$\mathscr{I}_1'(f) = \mathscr{I}_0'(f)\mathscr{T}(f) \quad (29)$$

where the primed quantities indicate normalization. Following Cerrina's treatment (59) of the limiting effect of statistical noise on spatial resolution, we study the signal levels in the image. Since the intensity is measured as a count rate, the signal $\mathscr{S}$ is obtained by multiplying $\mathscr{I}_1'$ by the counting time Δt. Then, the background can be taken into account in the same fashion, and the total signal may be written as

$$\mathscr{S}_T = \mathscr{S}_R + \mathscr{S}_B \quad (30)$$

$$= (\mathscr{I}_{0,R}'\mathscr{T} + \mathscr{I}_{0,B}'\mathscr{T})\,\Delta t \quad (31)$$

where subscripts R and B refer to the "real" and background signals, respectively. In order to resolve a feature, $\mathscr{S}_R$ must be higher than the noise level. This can be quantified by

$$\mathscr{S}_R = \mathscr{S}_T - \mathscr{S}_B \ge n(\sigma_T + \sigma_B) \quad (32)$$

where n is a positive nonzero integer indicating the level of confidence and σ_T and σ_B are the noise levels in the total and background signals, respectively.

Because Poisson's distribution describes statistical noise, for N counts a random noise of $\sqrt{N}$ will be observed. Then we may substitute $\sqrt{\mathscr{S}_T}$ and $\sqrt{\mathscr{S}_B}$ for σ_T and σ_B, respectively. After defining the signal-to-noise ratio R as $\mathscr{I}_{0,R}'/\mathscr{I}_{0,B}'$ we may write

$$\mathscr{S}_R \ge \frac{n^2}{\mathscr{T}}\left(\sqrt{1+\frac{1}{R}} + \sqrt{\frac{1}{R}}\right)^2 \quad (33)$$

For a small signal-to-noise ratio ($R \ll 1$), then, we may write the real object frequency distribution $\mathscr{I}_{0,R}'$ as

$$\mathscr{I}_{0,R}'(f) \ge \frac{4n^2}{\mathscr{T}(f)\,\Delta t\,R} \quad (34)$$

With the help of Eq. (28), we may solve this for the frequencies transmitted by an idealized incoherent optical system of circular aperture in the presence of statistical noise. We obtain

$$f \le f_0\left(1 - \frac{4n^2}{\mathscr{I}_{0,R}'\,\Delta t\,R}\right) \quad (35)$$

which shows that the maximum distinguishable frequency passed by a system with statistical noise is reduced, thus increasing the minimum period resolvable and hence decreasing the resolution. If the counting time Δt is sufficiently long for the desired level of confidence n, this frequency will approach the pure incoherent cutoff frequency for a diffraction-limited system. The counting time is directly related to the absolute intensity level of the image, which in turn is related to the brightness. This is true not just for incoherent scanning systems, but for X-ray microscopes in general, as long as there is no significant temporal oscillation in the true signal or the noise.

Importance of Brightness. Brightness is often defined for synchrotrons and insertion devices as the number of photons per unit time per unit angle per unit area per unit fraction of bandwidth (typical units are photons/s $\cdot$ mrad^2 $\cdot$ mm^2 $\cdot$ 0.1%). Without deriving expressions for the brightness in specific cases, we simply note that it is a measure of the ability of a source to illuminate a small area with small angular divergence. Clearly a high-brightness source (such as a third-generation synchrotron and its insertion devices) results in more incident flux per unit area on the sample in a X-ray microscope using that source. In a sequential imaging system such as a scanning microscope, this higher flux automatically means that the intensity level goes up, and thus, for a given counting time Δt, the signal goes up. Hence, better resolution can be obtained for the same optical system by counting for the same amount of time if all other parameters remain the same. In a parallel-imaging X-ray microscope such as the PEEM, although the X rays are not focused to a microspot, the electrostatic optics accept only those photoelectrons from a small area of the sample whose size is determined by the field of view for different magnifications and potentials of the optical column, the signal also increases.

Thus, the brighter the source is, the greater is the incident X-ray intensity on the area of interest, the higher the signal level in the photoelectron image, and the greater the capability to acquire spectra from small regions in reasonable real time. This time is longer for nonsynchrotron X-ray sources such as plasma point sources, which have a lower-flux output. The actual intensity at the image depends on various factors, including detector efficiency, sample quantum efficiency, acquisition time, and source brightness. Brightness can overcome shortcomings in the efficiencies and dramatically reduce the acquisition time, thus enabling higher spectromicroscopic resolution. This includes the ability to acquire higher-energy-resolution spectra from the samples, with a concurrent high spatial resolution. With fourth-generation synchrotrons like SOLEIL (France) and SLS (Switzerland) in the offing, the future of X-ray microscopy shines only brighter.

BIBLIOGRAPHY

1. T. A. Hall, H. O. E. Rockert, and R. L. deC. H. Saunders, *X-ray Microscopy in Clinical and Experimental Medicine,* Springfield, IL: Charles C. Thomas Publisher, 1972.
2. A. Moewes, Lumineszenz-Rastermikroskopie im Bereich weicher Röntgenstrahlung, Ph.D. thesis, Universität Hamburg, 1994.
3. B. K. Agarwal, *X-Ray Spectroscopy: An Introduction,* 2nd ed., New York: Springer-Verlag, 1991.
4. J. B. Vukovic and R. Antanasijevic, X-ray microscopy today, *Radiat. Meas.,* **28**: 817, 1997.
5. J. Stöhr, *NEXAFS Spectroscopy,* New York: Springer-Verlag, 1992.
6. R. N. Watts et al., A transmission x-ray microscope based on secondary-electron imaging, *Rev. Sci. Instrum.,* **68**: 3464, 1997.
7. M. Cardona and L. Ley (eds.), *Photoemission in Solids I: General Principles,* Vol. 1, New York: Springer-Verlag, 1978.
8. W. Meyer-Ilse et al., New high-resolution zone plate microscope at Beamline 6.1 of the ALS, *Synchrotron Radiat. News,* **8**: 29, 1995.
9. J. M. Heck et al., Resolution determination in x-ray microscopy: An analysis of the effects of partial coherence and illumination spectrum, *J. X-Ray Sci. Technol.,* 1998.
10. F. Vollrath, E. Sogaard, and J. T. Moller, X-ray microscopy in Aarhus, in J. Thieme et al. (eds.), *X-Ray Microscopy and Spectromicroscopy,* New York: Springer-Verlag, 1997.
11. M. Mundschau, Photoelectron emission microscopy, *Synchrotron Radiat. News,* **4**: 29, 1991.
12. W. Engel et al., A UHV-compatible photoelectron emission microscope for applications in surface science, *Ultramicroscopy,* **36** (1–3): 148, 1991.
13. B. P. Tonner and G. R. Harp, Photoelectron microscopy with synchrotron radiation, *Rev. Sci. Instrum.,* **59**: 853, 1988.
14. B. P. Tonner and D. Dunham, Sub-micron spatial resolution of a micro-XAFS electrostatic microscope with bending magnet radiation: Performance assessments and prospects for aberration correction, *Nucl. Instrum. Methods A,* **347**: 436, 1994.
15. B. P. Tonner et al., The development of electron spectromicroscopy, *J. Electron Spectrosc. Relat. Phenom.,* **75**: 309, 1995.
16. D. Dunham et al., Evaluation of aberration coefficients of practical electrostatic lenses for x-ray absorption micro-spectroscopy and imaging, *Nucl. Instrum. Methods A,* **347**: 441, 1994.
17. B. P. Tonner, Energy-filtered imaging with electrostatic optics for photoelectron microscopy, *Nucl. Instrum. Methods A,* **231**: 60, 1990.
18. G. De Stasio et al., MEPHISTO: Performance tests of a novel synchrotron imaging photoelectron spectromicroscope, *Rev. Sci. Instrum.,* **69**: 2062, 1998.
19. B. P. Tenner et al., A photoemission microscope with a hemispherical capacitor energy filter, *J. Electron Spectrosc. Relat. Phenom.,* **84**: 211–229, 1997.
20. S. Singh, X-ray photoemission spectromicroscopy and its application to the study of patterned titanium silicide, Ph.D. thesis, Univ. of Wisconsin, Madison, 1996.
21. S. Singh et al., An x-ray spectromicroscopic study of the local structure of patterned titanium silicide, *Appl. Phys. Lett.,* **71**: 55, 1997.
22. D.-B. Kao et al., Two-dimensional effects in titanium silicidation, *IEEE Trans. Electron Devices,* **45**: 187, 1998.
23. J. Stöhr et al., Element-specific magnetic microscopy with circularly polarized x-rays, *Science,* **259**: 658, 1993.
24. B. P. Tonner et al., Imaging magnetic domains with the x-ray dichroism photoemission microscope, *Nucl. Instrum. Methods A,* **347**: 142, 1994.
25. S. Jakubith et al., Spatiotemporal concentration patterns in a surface reaction: Propagating and standing waves, rotating spirals, and turbulence, *Phys. Rev. Lett.,* **65**: 3013, 1990.
26. G. Ertl, Oscillatory kinetics and spatio-temporal self-organization in reactions at solid surfaces, *Science,* **254**: 1750, 1991.
27. P. Pianetta et al., Core level photoelectron microscopy, *J. Electron Spectrosc. Relat. Phenom.,* **52**: 797, 1990.
28. P. Pianetta et al., Core level photoelectron microscopy with synchrotron radiation, *Rev. Sci. Instrum.,* **60**: 1687, 1989.
29. G. D. Waddill et al., Photoelectron microscopy and spectroscopy using synchrotron radiation, *J. Vac. Sci. Technol. A,* **9**: 1634, 1991.
30. T. Komeda et al., Photoelectron microscopy and spectroscopy of $Bi_2Sr_{2-x}Ca_{1-x}Cu_2O_{8+y}$(100), *Phys. Rev. B,* **43**: 8713, 1991.
31. G. Schmahl et al., X-ray microscopy of biological specimens with a zone plate microscope, *Ann. N.Y. Acad. Sci.,* **342**: 368, 1980.
32. J. Kirz, X-ray microscopy, *Synchrotron Radiat. News,* **4**: 17, 1991.
33. H. Rarback et al., The scanning transmission microscope at the NSLS, *Nucl. Instrum. Methods A,* **291**: 54, 1990.
34. J. Kirz, C. Jacobsen, and M. Howells, Soft x-ray microscopes and their biological applications, *Q. Rev. Biophys.,* **28**: 33, 1995.
35. H. Ade, NEXAFS microscopy of polymeric samples, *Synchrotron Radiat. News,* **7**: 11, 1994.
36. H. Ade et al., X-ray microscopy in polymer science: Prospects of a "new" imaging technique, *Polymer,* **36**: 1843, 1995.
37. H.-J. Shin, Personal communication, 1996.
38. H. Ade et al., Images of a microelectronic device with the X1-SPEM, a first generation scanning photoemission microscope at the National Synchrotron Light Source, *J. Vac. Sci. Technol. A,* **9**: 1902, 1991.
39. M. P. Kiskinova, *ESCA Microscopy of Surfaces and Interfaces with Submicron Spatial Resolution.* New York: Materials Research Society, 1998.
40. E. Di Fabrizio et al., High-performance multilevel blazed x-ray microscopy Fresnel zone plates: Fabricated using x-ray lithography, *J. Vac. Sci. Technol. B,* **12**: 3979, 1994.
41. W. Yun et al., Design of a dedicated beamline for x-ray microfocusing- and coherence-based techniques at the Advanced Photon Source, *Rev. Sci. Instrum.,* **67**: 3373, 1996.
42. W. B. Yun, *X-ray Microscopy Applications to Materials Science,* New York: Materials Research Society, 1998.
43. W. Rodrigues et al., X-ray microdiffraction studies of an integrated laser-modulator system, **417**: 161, 1997.
44. K. Ninomiya et al., Fabrication of an axisymmetric Wolter type I mirror with a gold deposited surface, *Jpn. J. Appl. Phys.,* **28**: 2303, 1989.
45. M. Hasegawa et al., Fabrication of Wolter-type x-ray focusing mirror using epoxy resin, *Rev. Sci. Instrum.,* **65**: 2568, 1994.
46. Photon Factory activity report, The Photon Factory synchrotron, Tsukuba, Japan, 1996, p. c11.
47. K. Ninomiya and M. Hasegawa, Scanning photoelectron microscope with submicron lateral resolution using a Wolter-type x-ray focusing mirror, *J. Vac. Sci. Technol.,* **13**: 1224–1228, 1995.
48. M. Hasegawa, A. Yoneyama, and K. Ninomiya, Soft x-ray scanning photoelectron microscope using Wolter-type focusing mirror, *J. Electron Spectrosc. Relat. Phenom.,* **80**: 361, 1996.
49. R.-P. Haelbich, Untersuchung der Eigenschaften von Mehrschichtinterferenzspiegeln aus absorbierenden Materialien und ihre Verwendung in einem Raster-mikroskop für weiche Röntgenstrahlung. Ph.D. thesis, Universität Hamburg, 1980.

50. I. Lovas et al., Design and assembly of a high-resolution Schwarzschild microscope for soft x-rays. *High Resolution Soft X-ray Optics, Proc. SPIE* **316**: 90, 1981.
51. W. Ng et al., High resolution spectromicroscopy reaches the 1000 Å scale, *Nucl. Instrum. Methods A,* **347**: 422, 1994.
52. K. Murakami et al., Schwarzschild microscope for carbon $K\alpha$ radiation, *Appl. Opt.,* **32**: 7057, 1993.
53. K.-J. Kim, Brightness, coherence and propagation characteristics of synchrotron radiation, *Nucl. Instrum. Methods A,* **246**: 71, 1986.
54. D. Attwood, New opportunities at soft-x-ray wavelengths, *Phys. Today,* **45** (8): 24–31, 1992.
55. M. Born and E. Wolf, *Principles of Optics,* New York: Pergamon, 1959, Chaps. 9, 10.
56. J. W. Goodman, *Introduction to Fourier Optics,* San Francisco, CA: McGraw-Hill, 1968, Chap. 6, p. 103.
57. J. W. Goodman, *Introduction to Fourier Optics,* San Francisco, CA: McGraw-Hill, 1968, Chap. 6, pp. 134–135.
58. J. W. Goodman, *Introduction to Fourier Optics,* San Francisco, CA: McGraw-Hill, 1968, Chap. 6, pp. 119–120.
59. F. Cerrina, X-ray photo-electron spectromicroscopy, *J. Electron Spectrosc. Relat. Phenom.,* **76**: 9, 1995.
60. K. Shinohara et al. (eds.), *X-ray Microscopy in Biology and Medicine,* Tokyo: Springer Verlag, 1990.
61. P.-C. Cheng and G.-J. Chen (eds.), *X-ray Microscopy: Instrumentation and Biological Applications,* Heidelberg: Springer Verlag, 1987.
62. G. Margaritondo, *Introduction to Synchrotron Radiation,* New York: Oxford University Press, 1988.
63. E.-E. Koch (ed.), *Handbook of Synchrotron Radiation,* New York: North Holland, Vols. 1–4, 1983–1991.
64. D. Sayre et al. (eds.), *X-ray Microscopy II,* Berlin: Springer Verlag, 1988.
65. C. J. Jacobsen and J. E. Trebes (eds.), Soft X-ray microscopy, *Proc. SPIE,* 1741, 1993.
66. W. Yun (ed.), X-ray microbeam technology and applications, *Proc. SPIE,* 2516, 1995.
67. W. Meyer-Ilse, X-ray microscopy and microanalysis, *Encyclopedia of Applied Physics,* VCH Publishers, Inc., in press, 1998.
68. F. Gozzo, Personal communication, 1998.
69. H. Solak et al., An x-ray spectromicroscopic study of electromigration in patterned Al(Cu) lines, *Appl. Phys. Lett.,* in press, 1998.

SANGEET SINGH-GASSON
University of Wisconsin—Madison

X WINDOWS. See WINDOWS SYSTEMS.